Critical analysis of in-plane free-space light beam coupling using photonic curved micromirrors

Yasser M Sabry, Mazen Erfan, Diaa Khalil, Tarik Bourouina

Critical analysis of in-plane free-space light beam coupling using photonic curved micromirrors

Yasser M. Sabry[a,*], **Mazen Erfan**[a,b,c], **Diaa Khalil**[a,b] **and Tarik Bourouina**[c]

[a]Ain Shams University, Electronics and Communications Engineering Department, Faculty of Engineering, Cairo, Egypt
[b]Si-Ware Systems, Cairo, Egypt
[c]Université Gustave Eiffel, ESYCOM, CNRS UMR 9007, ESIEE Paris, Noisy-le-Grand, France

Abstract. Free-space coupling of Gaussian light beams using flat and curved photonic micro-electromechanical systems mirrors was analyzed in detail. The theoretical background and the non-ideal effects, such as limited micromirror extent, asymmetry in the curvature of spherical micromirrors, misaligned axes, and micromirror surface irregularities, were analyzed. The derived formulas were used to study and compare theoretically and experimentally the behavior of flat (one-dimensional), cylindrical (two-dimensional), and spherical (three-dimensional) micromirrors. The analysis focused on the regime of dimensions in which the curved micromirrors radius of curvature is comparable to the incident beam Rayleigh range, also corresponding to a reference spot size. A transfer matrix-based field and power coupling coefficients were derived for general micro-optical systems accounting for different matrix parameters in the tangential and sagittal planes of the microsystem taking into account the possible non-idealities. The results were presented in terms of normalized quantities such that the findings are general and can be applied to different situations. In addition, silicon micromirrors were fabricated with controlled shapes and used to experimentally analyze the coupling efficiency at the visible and near-infrared wavelengths. [DOI: 10.1117/1.JOM.2.3.034001]

Keywords: coupling efficiency; curved micromirrors; Gaussian beams; micro-optics; optical microsystem; overlap integral.

Paper 21028G received Dec. 28, 2021; accepted for publication Jun. 21, 2022; published online Jul. 9, 2022.

1 Introduction

Microfabricated optical elements are interesting and used to process free-space optical beams propagating parallel to their supporting substrate in an ultra-compact, integrated optical bench configuration.[1,2] This concept was initially introduced based on the use of polycrystalline silicon thin films as a structural material with an additional metal coating to reach good reflectivity. In this approach, mechanical stress gradient in the resulting bimorph[3] and related bowing of the optical elements were found to be limiting factors that affected the optical performance. Therefore, it is tempting to extend this concept of a micro-optical bench to single-crystalline silicon, which offers unique capabilities such as monolithic coating-free all-silicon mirrors produced by micromachining single-crystalline silicon, resulting for instance in Bragg reflectors in the form of silicon walls separated by air trenches,[4,5] similar to one-dimensional (1D) photonic crystals but with enough depth to enable manipulating free-space propagating light. Furthermore, single-crystalline silicon has low absorption in the near-infrared and low thermoelastic loss,[6] which is of primary importance in optomechanics[7] for reaching high-quality factors in both the mechanical and the optical domains.

*Address all correspondence to Yasser M. Sabry, yasser.sabry@eng.asu.edu.eg

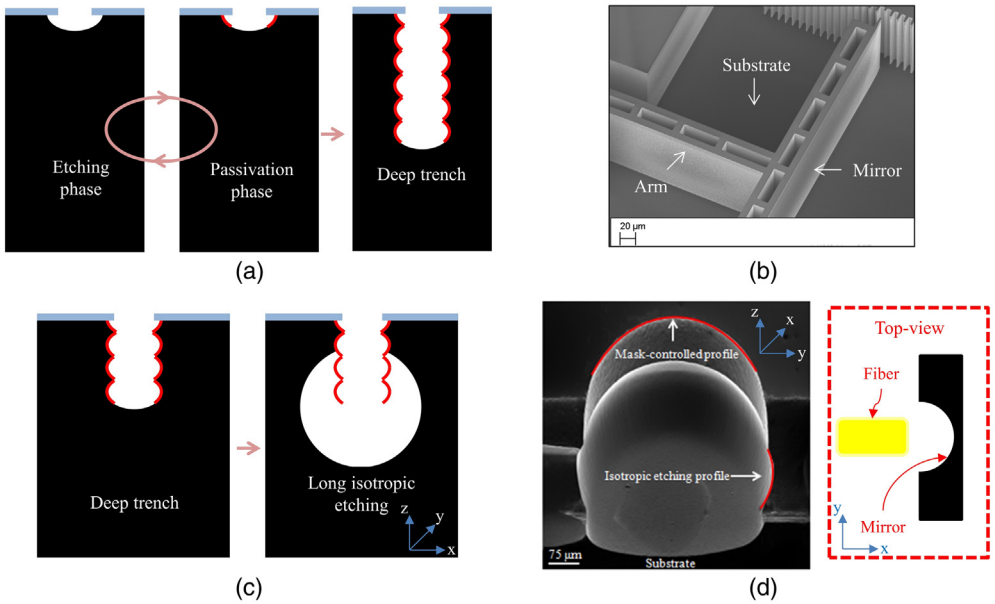

Fig. 1 (a) The DRIE Bosch process is an alternation between etching and passivation phases until a deep trench is etched into a substrate. (b) A SEM image for silicon-etched flat micromirror. (c) The 3D silicon etching combining DRIE and long isotropic etching. (d) A SEM for silicon-etched spherical micromirror.

Currently, deep reactive ion etching (DRIE) technology is being extensively used to achieve such optical benches from single-crystal silicon in a compact monolithic block.[8,9] Silicon-on-insulator (SOI) substrates are used to this end. One of the first SOI-based micro-optical benches implementing a vertical micromirror was introduced in 1997 by Marxer et al. for fiber optics switching applications.[10,11] Deeply etched micro-optical benches have the advantages of robustness and lithographic self-alignment of the microcomponents. Following the simple moving micromirror switch of Marxer, more complicated microengines and miniaturized systems have been developed; optical tunable filters,[12–14] two- and multiple-beam interferometers,[15–19] external cavity tunable lasers,[20,21] Fourier-transform spectrometers,[22–24] and optical scanner[25] are a few examples. The new research directions are focused mainly on the realization and use of microengines and miniaturized instrumentation in biology, chemistry, physics, and materials science. DRIE of silicon is the core technology for producing SOI-based micro-optical benches. An intensive review of the different DRIE processes can be found in Ref. 26; the general concept is shown in Fig. 1(a), and a scanning electron microscope (SEM) image of a flat micromirror typically etched in silicon using DRIE is shown in Fig. 1(b).

Free-space optical coupling is a critical performance feature in micro photonic components. Coupling elements are usually designed to mitigate optical beam divergence phenomena associated with Gaussian beam propagation and to achieve phase/mode matching. Deeply etched micro-optical benches comprise optical elements that are flat in the direction perpendicular to the wafer surface; i.e., out-of-plane direction. Silicon micromirrors were reported in both flat and cylindrical shapes, where the curved profile is formed in-plane with the respect to the substrate.[27,28] The allowable optical path was limited to tens of micrometers by the rapid decay of the coupling efficiency. Moreover, deeply etched micromirrors usually have a limited height. The limitation arises from the difficulty in maintaining high-quality vertical surface progressing deeply in plasma etching.[26] Thus, the height of the micromirrors is usually limited to 70 to 80 μm.[1–24] Beyond this limit, the verticality of the etched surface deteriorates with a highly negative profile and significantly rough surface. More advanced fabrication techniques have been applied to increase the depth of the micromirrors.[29–31] Therefore, optical beam truncation effects in micro-optical systems can be non-negligible, which further reduces the coupling efficiency below the ideal value as will be detailed in this paper.

High coupling efficiency with sub-millimeter optical path optical benches was achieved with the use of lenses fibers,[32] the assembly of a ball lens with flat mirrors,[33] the insertion of a fiber rod

lens with cylindrical mirrors,[21,34,35] or the hybrid integration of three-dimensional (3D) mirrors that require further assembly or mounting steps.[36,37] The 3D curved silicon micromirrors with in-plane optical axes were recently reported, as a monolithic solution, based on a fabrication process combining deep as well as isotropic etching of silicon.[38,39] The in-plane profile of the micromirror is defined using a lithographic process and the subsequent DRIE [see Fig. 1(c)]. Then, long isotropic etching is applied to form the micromirror curvature in the out-of-plane direction. A SEM image of a spherical micromirror etched in silicon is shown in Fig. 1(d). The surface of the micromirror is likely to be rotationally asymmetric due to the independent control of its curvature in two orthogonal directions. This can result as an artifact in micromirror fabrication or on purpose for engineering the coupling efficiency behavior of the micromirror. In addition to this asymmetry, the radii of curvature produced by this method are usually limited to a few hundred of micrometers, which is comparable to the processed Gaussian beam parameters. Both effects are analyzed in this paper.

The surface roughness of silicon-etched micromirrors is controlled by optimizing the DRIE process and by optionally reducing the cycles' time.[40,41] Techniques for smoothing out the DRIE Bosch process scallops from the resulting surface based on oxidation followed by oxide etching or using short anisotropic wet etching have been proposed.[42–44] The combination of a continuous isotropic reactive ion etching (RIE) etching process together with the DRIE Bosch process was used to produce a smooth micromirror's surface at the top part of the micromirror.[12] Local milling out the scallops of the DRIE after etching was carried out by means of a focused ion beam.[45] For more stringent verticality and smoothness requirements, the micromirrors were etched in a (110) wafer with the mask aligned to the (111) crystal planes.[46] In the latter case, wet anisotropic etching yielded very high surface quality and a vertical surface close to ideal on the expense of restricting the orientation of the flat micromirrors and prohibiting the proper etching of curved micromirrors. Therefore, the production of flat and curved micromirrors etched in silicon, in most of the cases, is accompanied by unavoidable surface roughness, which affects the efficiency of coupling using these micromirrors.

Depending on the spot size of the optical beam, lateral/angular shifts in the order of sub micrometer/degree resulting from micromirrors fabrication tolerance can be enough to cause significant reduction in the optical performance of high-finesse cavities.[47,48] Although several passive and active alignment technique have been introduced,[49–52] alignment of the components is still an issue in micro-optical systems. The impact of misalignment between the axis of single-mode (SM) fibers; i.e., Gaussian beam coupling, was first introduced by Marcuse and followed by several reports[53–58] usually focused on stigmatic Gaussian beams.[53,54] The coupling efficiency between two SM fibers was studied in Ref. 55 in the presence of fiber-tip lenses or a gradient-index rod lens to improve the coupling efficiency.[56–58] In addition to the prior work focused on general Gaussian beams in optical fibers or coupling via lenses, there are other works on coupling via microelectromechanical systems (MEMS) involving either optical switches or MEMS mirrors.[59–62] In this paper, we treat the impact of misalignment between the incident beam, generalized to astigmatic Gaussian beam, and the principal axis of the micromirror with different matrix parameters (i.e., mirror surface profiles) in two orthogonal planes providing a general solution for the coupling efficiency.

The micromirror has many applications with flat micromirrors being widely used in monolithic miniaturized optical benches, for instance, in $1 \times N$ and $N \times N$ cross couplers,[63] variable optical attenuators[64] and optical interferometers.[65] The height of the micromirrors is usually limited to 70 to 80 μm.[1–24] Beyond this limit, the verticality of the etched surface deteriorates with a highly negative profile and significantly rough surface. Deeper micromirrors were reported using alkaline etching, which restricts the surface profile and orientation.[29–31] Recently, the introduction of high throughput micromirrors with 150 to 300 μm depth was reported to overcome this type of loss[66,67] and enhance the profile of the reflected beam for optical scanning applications.

The utilization of cylindrical micromirrors in miniaturized optical benches has been reported in the literature from time to time to improve the coupling efficiency.[21,27] Engineering the curvature of the micromirror surface was reported as a way to improve the properties of Gaussian beam transformation using the curved micromirror.[25] The cross section of the surface in the out-of-plane direction is still flat etched using DRIE, and thus, an upper limit for the coupling efficiency of the micromirrors is encountered, as will be shown in Sec. 4.2. Despite this, it has

been used recently in different applications such as a multi-pass gas cell for gas analysis[68] and visible-laser generation on a silicon chip[69] due to the use of a slotted cylindrical micromirror in which its coupling efficiency is studied in detail in Ref. 70.

Silicon-etched spherical micromirrors were reported in both cases of having an out-of-plane or in-plane optical axis in many applications including single-atom detection, optical cavities and tunable lasers, and optical interconnects in addition to vertical coupling.[71–74] The main purpose was to have an efficient coupling mechanism. It is noteworthy that silicon curved micromirrors fabricated on a wafer top surface were also reported using isotropic chemical etching for the purpose of optical detection of a single atom,[71] a selective polishing method on the top of MEMS tunable vertical-cavity surface-emitting lasers (VCSEL),[72] and ion beam irradiation followed by electrochemical etching for cavity-quantum electro dynamics (QED) studies as well as optical interconnects.[73] In all of these techniques, the micromirror's optical axis is always out-of-plane with respect to the wafer substrate, which renders the fabricated micromirror incompatible with the silicon micro-optical bench concept in which the flat surface of the mirrors and the mechanical components is perpendicular to the wafer substrate.

In this paper, the free-space coupling of in-plane Gaussian beams using micromirrors is analyzed emphasizing the regime of dimensions, in which the curved micromirror radius of curvature/aperture is comparable to the incident Gaussian beam Rayleigh range/spot size. In addition, the analysis accounts for the non-idealities involved in the process of coupling as well [see Figs. 2(a)–2(f)]. First, a generalized analytical expression for the coupling efficiency is derived in Sec. 2 based on the overlap integral and transfer matrix analysis. The expression can

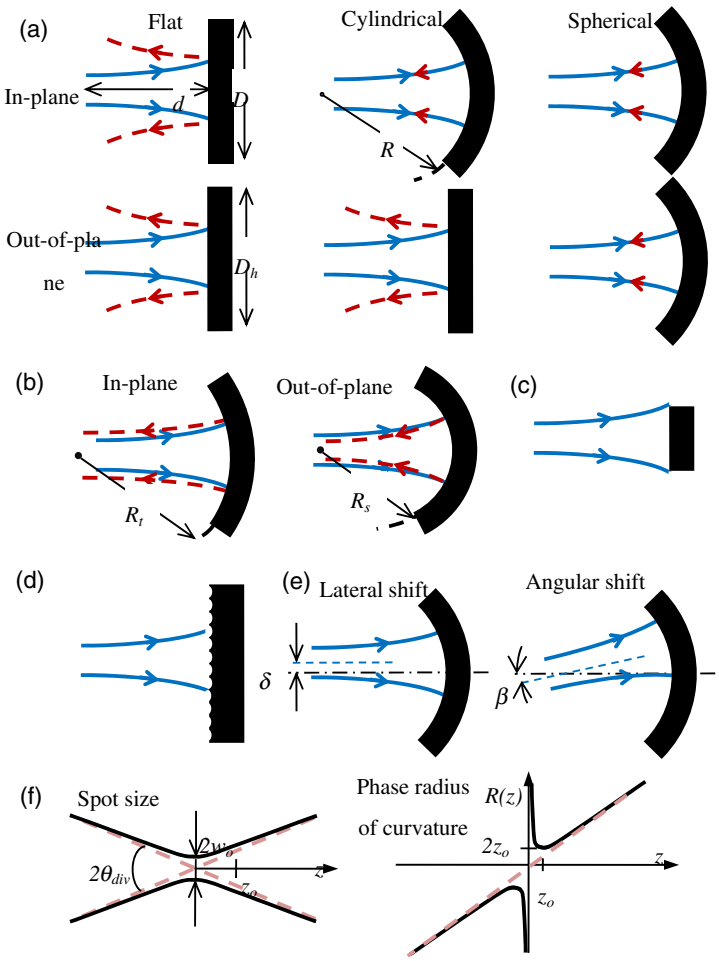

Fig. 2 Schematic illustration for the coupling cases under study. (a) Flat versus curved micromirrors. (b) Asymmetrical curved micromirrors. (c) Limited micromirror size. (d) Micromirror surface roughness. (e) Lateral and angular misalignment. (f) Gaussian beam propagation properties.

be applied to any micro-optical system once its transfer matrix parameters are known in the tangential and sagittal planes. The expression accounts for astigmatic Gaussian beams as well. In Sec. 3, a measurement technique based on using a cleaved SM optical fiber for coupling measurements is presented to account for the possible Fabry–Pérot weak effect between the fiber end face and the micromirror surface. In Sec. 4, coupling by flat (1D), cylindrical [two-dimensional (2D)], and spherical (3D) micromirrors is thoroughly analyzed theoretically and proven experimentally based on the theoretical basis and measurement method introduced in Secs. 2 and 3, respectively. Throughout the whole of our discussion, parameter normalization is used such that the findings are independent of the specific values of the operating wavelength and the Gaussian beam parameters.

2 Theoretical Framework of the Coupling Efficiency

The field coupling coefficient between a normalized incident Gaussian beam and another Gaussian beam reflected back from (or transmitted through) an optical system is given by the well-known overlap integral:[53,75]

$$k = \iint E_i E_r^* \mathrm{d}A = \frac{2j\lambda}{\pi}\left[w_{it}w_{is}w_{rt}w_{rs}\left(\frac{1}{q_{it}^*}-\frac{1}{q_{rt}}\right)\left(\frac{1}{q_{is}^*}-\frac{1}{q_{rs}}\right)\right]^{-0.5}, \tag{1}$$

where the subscripts i and r stand for the incident and reflected Gaussian beams, respectively, w is the spot radius, q is the complex phase radius of curvature, and the subscripts t and s stand for the tangential and sagittal planes, respectively. For an optical system with different properties in the tangential and sagittal planes, the reflected and incident beams are related by a transfer matrix in the form

$$M = \begin{bmatrix} A_t & 0 & B_t & 0 \\ 0 & A_s & 0 & B_s \\ C_t & 0 & D_t & 0 \\ 0 & C_s & 0 & D_s \end{bmatrix}. \tag{2}$$

The transfer matrix in Eq. (2) with its sparse nature is applicable as long as the optical system understudy poses micromirror symmetry in the transverse directions.[76] The corresponding Gaussian beams complex phase radii are connected as

$$q_{rt,s} = \frac{A_{t,s}q_{it,s} + B_{t,s}}{C_{t,s}q_{it,s} + D_{t,s}}. \tag{3}$$

By assuming that the incident Gaussian beam has its waist location at the input plane of the optical system, where any offset can be accounted for in Eq. (2) without loss of generality, we have

$$q_{rt,s} = \frac{A_{t,s}q_{it,s} + B_{t,s}}{C_{t,s}q_{it,s} + D_{t,s}}, \tag{4}$$

$$w_i = w_o, \tag{5}$$

$$q_i = jz_o = j\frac{\pi w_o^2}{\lambda}, \tag{6}$$

$$\frac{1}{q_r} = \frac{jz_oC + D}{jz_oA + B} = \frac{z_o^2AC + BD - jz_o}{z_o^2A^2 + B^2}, \tag{7}$$

$$w_r = \sqrt{-\frac{\lambda}{\pi\,\mathrm{Im}(1/q_r)}} = \sqrt{\frac{\lambda(A^2z_o^2 + B^2)}{\pi z_o^2}}, \tag{8}$$

$$\frac{1}{q_i^*} - \frac{1}{q_r} = -\frac{jz_o(A+D) + B - Cz_o^2}{jz_oB - Az_o^2}, \tag{9}$$

where the condition $AD - BC = 1$ is incorporated to simplify Eq. (7). Substituting back into Eq. (1) yields the following expression for the field complex coupling coefficient:

$$k = \frac{\sqrt{2jz_{ot}}\sqrt{A_tz_{ot} - jB_t}}{(A_t^2z_{ot}^2 + B_t^2)^{0.25}\sqrt{jz_{ot}(A_t + D_t) + B_t - C_tz_{ot}^2}} \times \frac{\sqrt{2jz_{os}}\sqrt{A_sz_{os} - jB_s}}{(A_s^2z_{os}^2 + B_s^2)^{0.25}\sqrt{jz_{os}(A_s + D_s) + B_s - C_sz_{os}^2}}. \tag{10}$$

The expression derived in Eq. (10) contains information about both the phase and magnitude of the overlap integral, which is useful in situations in which interference between two or more beams occurs. The rest of this paper concentrates on the magnitude part. The power coupling efficiency is obtained by squaring the magnitude of the field coupling coefficient and is given by the following expression:

$$\eta = \frac{2z_{ot}}{\sqrt{B_t^2 + z_{ot}^2(A_t^2 + D_t^2 + 2) + z_{ot}^4C_t^2}} \frac{2z_{os}}{\sqrt{B_s^2 + z_{os}^2(A_s^2 + D_s^2 + 2) + z_{os}^4C_s^2}}. \tag{11}$$

The derived relation in Eq. (11) expresses the power coupling efficiency between the input and the output Gaussian beams to an optical system with known transfer matrix parameters in the system tangential and sagittal planes. The Gaussian beams can be of elliptical or circular cross section. In the case of elliptical beams, the incident beam and the optical system should have the same orientation of the tangential and the sagittal planes so that the transfer matrix preserves its sparsity. The expression in Eq. (10) can be applied to the cases of flat, cylindrical, and spherical micromirrors [Fig. 1(a)], including rotationally asymmetric micromirrors [Fig. 1(b)] with the aid of Table 1.

2.1 *Effect of Limited Micromirror Size*

In the presence of optical beam truncation [Fig. 2(c)], the coupling efficiency can be divided into three parts; the first of them is given by Eq. (11). The second part arises from the power escaped out of the micromirror physical dimension; i.e., not reflected. Finally, the third part is related to the additional coupling loss, which takes place as a result of the projection of the truncated beam on the fundamental Gaussian beam. It is shown that the latter two parts of the losses can be accounted for by squaring of the truncation power loss formula.[77] For a rectangular micromirror

Table 1 The transfer matrix elements connecting incident and reflected beams by flat, cylindrical, and spherical mirrors, where d is the distance between the incident beam waist and the micromirror (i.e., the optical path of the beam is $2d$).

Element	Flat micromirror	Cylindrical micromirror	Spherical micromirror
A_t	1	$1 - 2d/R_t$	$1 - 2d/R_t$
B_t	$2d$	$2d(1 - d/R_t)$	$2d(1 - d/R_t)$
C_t	0	$-2/R_t$	$-2/R_t$
D_t	1	$1 - 2d/R_t$	$1 - 2d/R_t$
A_s	1	1	$1 - 2d/R_s$
B_s	$2d$	$2d$	$2d(1 - d/R_s)$
C_s	0	0	$-2/R_s$
D_s	1	1	$1 - 2d/R_s$

of width D_w and height D_h typically encountered in micro-optical bench systems, the truncation power loss is given as[78]

$$K = \text{erf}\left(\frac{D_w}{\sqrt{2}w}\right)\text{erf}\left(\frac{D_h}{\sqrt{2}w}\right), \tag{12}$$

where erf is the error function and w is the spot radius of the Gaussian beam. Combining the square of Eq. (12) with Eq. (11), the overall coupling efficiency in the presence of truncation is given as

$$\eta_T = \eta\left[\text{erf}\left(\frac{D_w/w_o}{\sqrt{2+2(d/z_o)^2}}\right)\text{erf}\left(\frac{D_h/w_o}{\sqrt{2+2(d/z_o)^2}}\right)\right]^2. \tag{13}$$

where w was replaced by $w_o 1 + (d/z_o)^{20.5}$, with w_o being the radius of the beam at its waist and z_o being the Rayleigh range of the beam.

2.2 *Effect of Surface Roughness*

The existence of surface roughness [see Fig. 1(d)] directly impacts the coupling efficiency of the micromirror. In the beam coupling process, we are interested in specular reflection on the micromirror surface, in which light from a single incoming direction is reflected into a single outgoing direction, following the law of reflection of light. In the presence of surface irregularities, an amount of the incident light is scattered into other directions[79–83] and, thus, does not contribute to the coupling efficiency. The root mean square (RMS) roughness σ, usually defined as the square root of the standard deviation of surface topology from its mean value, is used to express the effect roughness on light scattering without considering the correlation length of the roughness. This is particularly true for the etched micromirrors when the micromirror surface is a slightly rough surface with respect to the wavelength; i.e., $\sigma/\lambda < 20$.[84] In this case, the reflectance of the micromirror is given as

$$R_m = R_i \exp(-16\pi^2\sigma^2/\lambda^2), \tag{14}$$

where R_i is the ideal reflectance of the micromirror when $\sigma = 0$. The ideal reflectance of the silicon micromirrors is usually improved either by etching multi-layer distributed Bragg grating micromirrors or by coating the silicon surface with a metal layer of about 50- to 100-nm thickness.[12,25,38] For silicon-air Bragg mirrors, the refractive index contrast is high, relative to the common multilayer mirrors fabricated by thin-film deposition, and so is the amount of scattered light. The use of the model of Carniglia[85] was proposed to treat this particular case by adding a single absorbing layer at each material interface as a function of its surface RMS roughness. The real part of the refractive index of the layer is given by Drude effective medium approximation, and an imaginary part is added to take into account the reduced transmission and reflection predicted by the scalar scattering theory. This approach was recently adopted in Ref. 86 and showed good agreement with the experimental results. Another approach is based on the overall phase transformation where the 3D mirror overall phase is divided into two components: the phase curvature responsible for the collimation of an optical beam and a random phase due to the surface roughness.[87] This is simulated using the Fourier optics approach, and the roughness effect is evaluated by calculating the coupling efficiency (overlap integral) between the resulting beam and the ideal beam.

2.3 *Effect of Lateral/Angular Misalignment*

Misalignment between the beam optical axis and the micromirror principal axis can be in the form of lateral shift δ or angular shift β. Consequently, there will be a shift misalignment Δ_c and an angular misalignment α_c between the incident and reflected Gaussian beams. These misalignments can be calculated from the problem geometry, and their effect on the field coupling coefficient is given as[75]

Table 2 Modified transfer matrix elements for Gaussian beam transformation in the presence of misalignment.

Element	Flat micromirror	Cylindrical micromirror	Spherical micromirror
A_t	1	$1-2d_2/R_t\cos(\theta_{\text{inc}})$	$1-2d_2/R_t\cos(\theta_{\text{inc}})$
B_t	d_1+d_2	$d_1+d_2-2d_1d_2/R_t\cos(\theta_{\text{inc}})$	$d_1+d_2-2d_1d_2/R_t\cos(\theta_{\text{inc}})$
C_t	0	$-2/R_t\cos(\theta_{\text{inc}})$	$-2/R_t\cos(\theta_{\text{inc}})$
D_t	1	$1-2d_2/R_t\cos(\theta_{\text{inc}})$	$1-2d_2/R_t\cos(\theta_{\text{inc}})$
A_s	1	1	$1-2d_2\cos(\theta_{\text{inc}})/R_s$
B_s	d_1+d_2	d_1+d_2	$d_1+d_2-2d_1d_2\cos(\theta_{\text{inc}})/R_s$
C_s	0	0	$-2\cos(\theta_{\text{inc}})/R_s$
D_s	1	1	$1-2d_2\cos(\theta_{\text{inc}})/R_s$

$$k_M = k\,\exp[-j\pi\lambda^{-1}\Delta_c^2(q_{rt}-q_{it}^*)^{-1}]\exp\left[j\pi\lambda^{-1}\alpha_c^2\left(\frac{1}{q_{rt}}-\frac{1}{q_{it}^*}\right)^{-1}\right]. \tag{15}$$

In addition to its direct impact on the coupling coefficient, misalignment of the incident Gaussian beam with the micromirror causes the beam to undergo a slightly different transformation from that described by the transfer matrix given in Table 1. The modified matrix parameters given in Table 2 should be used instead; these account for the incidence angle on the micromirror surface θ_{inc} and the difference in the propagation distances before and after reflection d_1 and d_2, respectively. The transfer matrix parameters in Table 2 were obtained assuming that the misalignment befalls in the tangential plane. Following a similar analysis to the one used to derive Eq. (11), the coupling efficiency in the presence of misalignment in the tangential plane between the incident beam and the micro-optical system is given as

$$\eta_M = \eta\,\exp\left[\frac{-2\pi\Delta_c^2}{\lambda}\frac{z_o(1+D_t^2)+C_t^2z_o^3}{[B^2+z_o^2(A_t^2+D_t^2+2)+z_o^4C_t^2]}-\frac{2\pi\alpha_c^2z_o(B_t^2+A_t^2z_o^2)}{\lambda(B_t^2+A_t^2z_o^2+z_o^2)}\right]. \tag{16}$$

Equation (16) can be used for any optical system once its transfer matrix parameters are known. A similar expression can be derived for the coupling efficiency in the presence of misalignment in the sagittal plane.

3 Measurement Method

The method used for measuring the coupling efficiency is based on using an SM optical fiber to generate the Gaussian beam incident on the micromirror and collects back the reflected beam as shown in Fig. 3.[38] Indeed, the transverse field distribution of the optical fiber fundamental mode, which is called the LP01 mode, can be approximated to a Gaussian profile within 1% accuracy as long as the V-number is in the range $1.2 < V < 2.4$.[53,84] This condition holds true in our experiments, in which Gaussian beams with Rayleigh ranges of 30 and 45 μm are generated using SM optical fibers with core radii of 2 and 4.5 μm at wavelengths of 675 and 1550 nm, respectively. To separate the reflected signal coupled back into the optical fiber, the fiber is fed from a laser source through an optical directional coupler, and the power coupled back is detected using an optical detector and current meter. The optical fiber is mounted on a micropositioner with 5-deg of freedom to ensure good alignment between the fiber and the micromirror, and the latter is mounted on a variable height post. Active alignment was applied to reach the best coupling efficiency due to the precision of the micropositioners with micrometer accuracy in the translational directions as well as 0.05 deg in the angles. The process of aligning the fiber and varying the distance between the fiber tip and the micromirror surface is performed with the aid of a microscope with a calibrated microscale. The calibration was carried out using a microscope

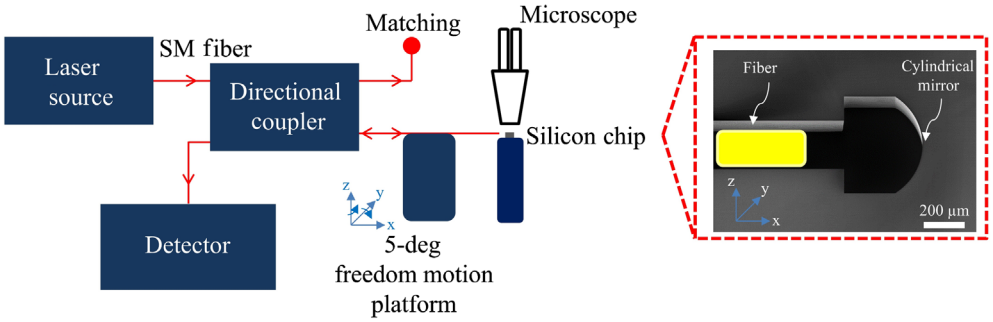

Fig. 3 Silicon micromirrors coupling efficiency measurements using SM optical fibers fed from monochromatic light source, a directional coupler, and an optical detector.

calibration slide. It is worth noting that the out-of-plane radii of curvature of the spherical MEMS mirrors can be measured from the SEM images as the ones shown in Fig. 1(d), where the scale in μm is used to determine the actual values. Regarding the cylindrical mirrors as those shown in Fig. 3, we can rely on the very high accuracy of the photolithography on having their radii of curvature as drawn on the mask design for fabrication.

A parasitic weak Fabry–Pérot cavity is formed between the optical fiber cleaved surface and the micromirror surface due to the refractive index mismatch at the fiber-air interface and the micromirror reflectance. Knowing that the fiber-air interface reflectance is much smaller than one, higher-order terms of the Fabry–Pérot cavity Airy-function response can be neglected, and thus, the detector power is given as

$$P \approx P_o\left[R_m T_f^2 \eta + R_f + 2\sqrt{R_f R_m} T_f \sqrt{\eta}\cos\left(\frac{2\pi}{\lambda} 2d + \varphi_k\right)\right], \tag{17}$$

where Po is a normalization factor depending on the source power and the directional coupler division ratio, R_f is the fiber-air interface reflectance, T_f is the fiber-air interface transmittance, and ϕ_k is the phase angle of the field coupling coefficient in Eq. (10). The variation of the cosine term is effective only within submicron resolution and, therefore, can be neglected. This is particularly applicable for working distance measurement, as in our case, and the cosine term is replaced by unity assuming that we are always seeking the peak value of the power P_{peak}. The coupling efficiency η can be extracted knowing the micromirror reflectance and fiber interface transmittance and reflectance. Rearranging Eq. (17) yields

$$\eta + \frac{2\sqrt{R_f}}{\sqrt{R_m} T_f}\sqrt{\eta} + \frac{R_f}{R_m T_f^2} - \frac{P_{\text{peak}}}{R_m T_f^2 P_o} = 0. \tag{18}$$

The solution of Eq. (18) for η is given as

$$\eta = \frac{P_{\text{peak}} + R_f P_o - 2\sqrt{P_o R_f}\sqrt{P_{\text{peak}}}}{R_m P_O T_f^2}. \tag{19}$$

4 Analysis of Micromirrors Coupling Efficiency

Theoretical and experimental analyses of flat, cylindrical, and spherical micromirrors coupling efficiency are presented in this section. The analysis is based on the theoretical basis and measurement method introduced in Secs. 2 and 3, respectively.

4.1 *Flat Micromirrors*

The expression for Gaussian beam coupling efficiency using flat micromirrors η_{F} is obtained by substituting with the appropriate transfer matrix parameters in Table 1 into Eq. (11). This substitution yields

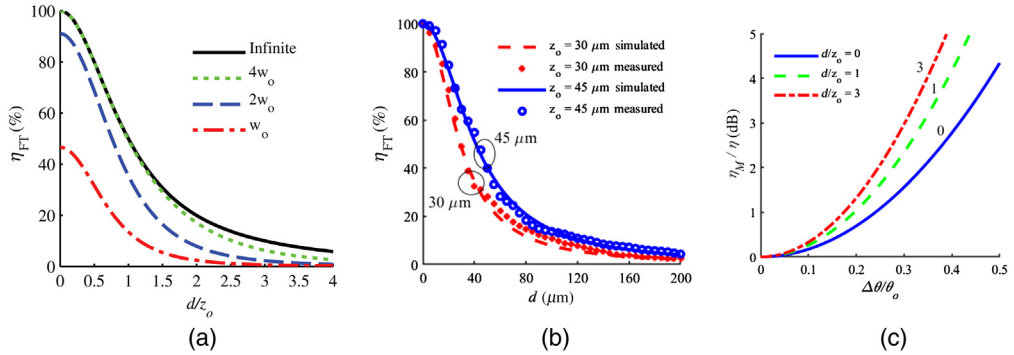

Fig. 4 Coupling efficiency of flat micromirrors. (a) The effect of truncation for micromirror heights of w_o, $2w_o$, $4w_o$, and infinite, and the micromirror width is infinite. (b) Theoretical (in lines) and experimental (in markers) date for $z_o = 30$ and 45 μm. (c) The loss in coupling efficiency of a flat micromirror versus the relative tilt misalignment for different d/z_o ratios.

$$\eta_F = \left[1 + \left(\frac{d}{z_o}\right)^2\right]^{-1}. \tag{20}$$

The coupling efficiency decays with a longer propagation distance, and the decay rate is more significant for a smaller beam Rayleigh range. The propagation distances corresponding to 1-, 3-, and 10-dB coupling loss are $d = 0.5z_o$, z_o, and $3z_o$, respectively. The coupling efficiency of flat micromirrors in the presence of truncation η_{FT} is obtained by replacing η by η_{F} in Eq. (13). The result is shown in Fig. 4(a). The width of the micromirror is kept large enough while its height—usually limited by the micromachining technology—is assigned the values of w_o, $2w_o$, $4w_o$, and infinite for comparison. The truncation loss is significant for the first two cases, whereas its effect can be neglected for the third case, unless $d > 1.5\, z_o$. Experimental data for the coupling efficiency was obtained, as shown in Fig. 4(b), using the measurement technique presented in Sec. 3 for a flat micromirror with a height of 150 μm and a width of 300 μm. The micromirror is aluminum metalized and has a reflectance of about 90%, which was used to extract the coupling efficiency with the aid of Eq. (19). The in-plane tilt angle between the optical fiber and the micromirror surface could be minimized using a long and narrow fiber groove aligned with micromirror in lithographic manner. The out-of-plane tilt angle alignment was carried seeking the maximum reflected power. Theoretical and experimental data are in a good agreement. The slight differences can be attributed to the uncertainty in the optical fiber mode-filed diameter and thus the beam Rayleigh range. In addition, a slight angular misalignment in the optical axis can result from the cleaving quality of the optical fiber surface. Error in the positioning scale of the opto-mechanical micropositioner and its hysteresis can be a third reason for the difference.

To assess the impact of angular misalignment on the coupling efficiency, Eq. (16) for a flat micromirror is put in the form

$$\eta_{\mathrm{FM}} = \eta_F \exp\left[-\frac{\Delta_c^2}{w_o^2}\frac{1}{1 + d^2/z_o^2} - \frac{\alpha_c^2}{\theta_o^2}\frac{1 + 4d^2/z_o^2}{1 + 2d^2/z_o^2}\right], \tag{21}$$

where d_1 is set equal to d_2. The expression in Eq. (21) assumes a small tilt angle misalignment, such that $\sin(\alpha_c) \approx \tan(\alpha_c) \approx \alpha_c$. This assumption simplifies the expression and enables the normalization of the involved quantities, which helps to gain insight into the dominant factors. It preserves the physical sense that a Gaussian beam with a wider beam waist is less sensitive to shift misalignment, whereas a beam with a larger divergence angle is less sensitive to angular misalignment. The impact of tilt misalignment on the coupling efficiency was studied for $d/z_o = 0$, 1, and 3. The quantities Δ_c/w_o and α_c/θ_o were deduced from the problem geometry to be $2(\Delta\theta/\theta_o)(d/z_o)$ and $2(\Delta\theta/\theta_o)$, respectively. The corresponding misalignment coupling loss is shown in Fig. 4(c). The coupling loss increases with increasing distance d between the incident beam waist and the micromirror surface. This is a direct result of the proportionality

between Δ_c and d. The rate of increment decreases with distance d as a result of the Gaussian beam expansion with propagation.

4.2 *Cylindrical Micromirrors*

The expression for Gaussian beam coupling efficiency using cylindrical micromirrors η_C is obtained by substituting with the appropriate transfer matrix parameters in Table 1 into Eq. (11). This substitution yields:

$$\eta_C = \left[1 + \left(\frac{d}{z_o}\right)^2\right]^{-0.5} \left[0.5 + \left(\frac{d}{z_o}\right)^2 \left(1 - \frac{d}{z_o}\frac{z_o}{R}\right)^2 + 0.5\left(1 - 2\frac{d}{z_o}\frac{z_o}{R}\right)^2 + \left(\frac{z_o}{R}\right)^2\right]^{-0.5}. \quad (22)$$

The first multiplication term in Eq. (22) represents the coupling efficiency in the sagittal plane due to the flat cross section of the micromirror surface. The second multiplication term expresses the coupling efficiency in the tangential plane accounting for the curvature in that plane. Indeed, Eq. (22) reduces to Eq. (20) when the radius of curvature is infinite. The truncation effect due to the finite size of the micromirror can be accounted for in a similar way as the flat micromirror. The second term in Eq. (22) has maxima versus d/z_o that can be found by means of partial differentiation and nulling of the derivative, which yields

$$\left(1 - 2\frac{d}{z_o}\frac{z_o}{R}\right)\left[\left(\frac{d}{z_o}\right)^2 - \frac{d}{z_o}\frac{R}{z_o} + 1\right] = 0. \quad (23)$$

Thus, the extremes are located at

$$d_{m1} = 0.5R, \quad (24)$$

$$d_{m2,3} = 0.5R\left(1 \pm \sqrt{1 - \left(\frac{2z_o}{R}\right)^2}\right). \quad (25)$$

A single extreme is found at d_{m1} when $z_o > R/2$, while two additional extremes are found at $d_{m2,3}$ when $z_o < R/2$. Back substitution in the second term of Eq. (22) when $z_o < R/2$ yields unity maxima for the $d_{m2,3}$ locations, whereas the maxima located at d_{m1} is smaller than unity. It is worth noting that for the specific case of a curved micromirror, the radius of curvature of the micromirror is comparable to the incident Gaussian beam Rayleigh range. In contrast to the flat micromirrors, the zero-distance coupling efficiency of the cylindrical micromirrors is always smaller than unity and is given as

$$\eta_C|_{d=0} = \left[1 + \left(\frac{z_o}{R}\right)^2\right]^{-0.5}. \quad (26)$$

The cylindrical micromirror coupling efficiency expressed in Eq. (22) is shown in Fig. 5(a) versus the ratio d/z_o for $z_o/R = 2$, 1, 0.5, and 0.25. The zero-distance coupling is much smaller than unity unless the ratio z_o/R is small enough, e.g., 0.25. There is only one peak location and close to zero when $z_o/R > 0.5$. For smaller z_o/R, the peaks located close to $d/z_o \approx R/z_o$ tend to be recognized. The coupling efficiency of the cylindrical micromirrors is non-satisfactory when efficient coupling is needed.

Experimental data for the coupling efficiency was obtained, as shown in Figs. 5(b) and 5(c), using the measurement technique presented in Sec. 3. Cylindrical micromirrors with radii of curvature of 50, 150, and 300 μm were used in this experiment. The height of the micromirrors is 150 μm, and their widths are 100, 300, and 600 μm, respectively. The micromirrors are aluminum metalized and have a reflectance of about 90%, which was used to extract their coupling efficiency with the aid of Eq. (19). In Fig. 5(b), the data are shown for the 150-μm radius micromirror using Gaussian beams with Rayleigh ranges of 30 and 45 μm. The coupling efficiency of the micromirrors with 50 and 300 μm radii of curvatures is shown in Fig. 5(c) using the 45-μm Rayleigh range Gaussian beam. There is an overall well-agreement between the experimental data and the theoretical expectation. The slight differences are attributed to the same issues

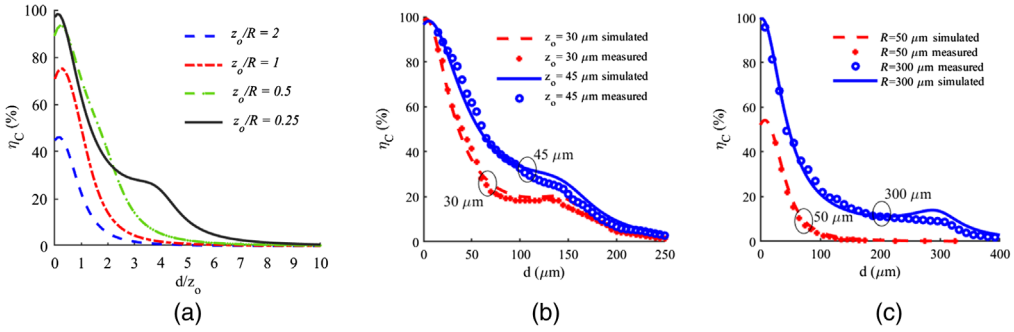

Fig. 5 Coupling efficiency of cylindrical micromirrors. (a) Theoretical data for different z_o/R ratios. (b) Theoretical (in lines) and experimental (in markers) data of 150-μm radius cylindrical micromirror for $z_o = 30$ and 45 μm. (c) Theoretical (in lines) and experimental (in markers) data of 50- and 300-μm radius cylindrical micromirrors for $z_o = 45$ μm.

mentioned in Sec. 4.1. Indeed, there are stringent requirements for the alignment in the case of curved micromirrors, as will be detailed in the next section.

4.3 *Spherical Micromirrors*

The coupling efficiency of rotation-symmetric spherical micromirrors η_S is obtained by substituting with the appropriate transfer matrix parameters in Table 1 into Eq. (11) and setting $R_s = R_t = R$:

$$\eta_S = \left[0.5 + \left(\frac{d}{z_o}\right)^2 \left(1 - \frac{d}{z_o}\frac{z_o}{R}\right)^2 + 0.5\left(1 - 2\frac{d}{z_o}\frac{z_o}{R}\right)^2 + \left(\frac{z_o}{R}\right)^2\right]^{-1}. \tag{27}$$

The expression is shown in Fig. 6(a) versus the ratio d/z_o for $z_o/R = 2$, 1, 0.5, and 0.25. Similar to cylindrical micromirrors, the zero-distance coupling efficiency is much smaller than unity unless the ratio z_o/R is small enough. The zero-distance coupling efficiency is given as

$$\eta_S|_{d=0} = \left[1 + \left(\frac{z_o}{R}\right)^2\right]^{-1}. \tag{28}$$

Unity coupling efficiency can be obtained when z_o/R is ≤ 0.5. The coupling efficiency at location d_{m1} is given as

$$\eta_S|_{d=d_{m1}} = \frac{1}{\frac{1}{2} + \frac{R^2}{16z_o^2} + \frac{z_o^2}{R^2}}. \tag{29}$$

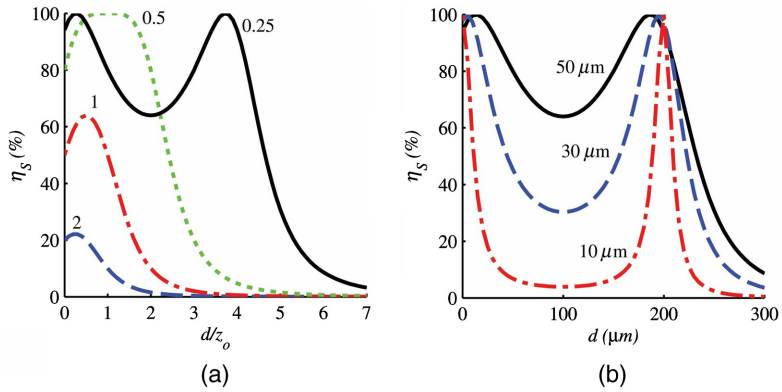

Fig. 6 Coupling efficiency of rotationally symmetric spherical micromirrors. (a) Theoretical data for different z_o/R ratios. (b) Theoretical data for $R = 200$ μm and $z_o = 1$, 30, and 50 μm.

The special case of $z_o/R = 0.5$ has a unique flat response centered on $d/z_o = 1$. The 1-dB width of the response extends from zero distance up to $d/z_o = 2$. Indeed, this response is very convenient to consider implementing a wide tuning mechanism for the micromirror position centered on $d/z_o = 1$ (i.e., $d = 0.5R$) with nearly a flat response over a distance $\Delta d = \pm z_o$. This is of particular interest for applications like optical delay lines and external cavity tunable lasers. For larger ratios of micromirror radius of curvature to beam Rayleigh range, there are two unity extremes at locations d_{m2} and d_{m3}, with the latter becoming closer to $d = R$ when z_o/R is much smaller than 0.5. For instance, consider the coupling efficiency shown in Fig. 6(b) for the case of $R = 200$ μm and the three values of Gaussian beam Rayleigh range of 10, 30, and 50 μm. The coupling efficiency curve around the extremes becomes sharper and the extremes' locations become weakly dependent on z_o when z_o/R is small enough. In such a situation, the spherical micromirrors pose the capability of efficiently coupling both the elliptical as well as the circular beams for a relatively wide wavelength range. From the application perspective, elliptical Gaussian beams are the typical output of semiconductor lasers, and the utilization of a wide bandwidth optical source is mandatory in low coherence applications.

The surface of the micromirror is likely to be rotationally asymmetric due to the independent control of its curvature in two orthogonal directions. This can result as an artifact in micromirror fabrication or on purpose for engineering the coupling efficiency behavior of the micromirror. Substituting with the appropriate transfer matrix parameters in Table 1 into Eq. (11) and assuming that $R_s \neq R_t$ yields the following expression for the coupling efficiency:

$$\eta_{SU} = \left[0.5 + \left(\frac{d}{z_o}\right)^2\left(1 - \frac{d}{z_o}\frac{z_o}{R_t}\right)^2 + 0.5\left(1 - 2\frac{d}{z_o}\frac{z_o}{R_t}\right)^2 + \left(\frac{z_o}{R_t}\right)^2\right]^{-0.5} \times \left[0.5 + \left(\frac{d}{z_o}\right)^2\left(1 - \frac{d}{z_o}\frac{z_o}{R_s}\right)^2 + 0.5\left(1 - 2\frac{d}{z_o}\frac{z_o}{R_s}\right)^2 + \left(\frac{z_o}{R_s}\right)^2\right]^{-0.5}. \quad (30)$$

For the purpose of evaluating the mismatch impact, the radii are assumed to be $R_s = R_o + \Delta R/2$ and $R_s = R_o - \Delta R/2$, where R_o is the mean value and ΔR is the total deviation. The coupling efficiency is depicted in Fig. 7(a) for the cases $z_o/R = 0.5$ and 0.25 with $\Delta R/R$ of 0.1 and 0.5. The mismatch causes deterioration in the coupling efficiency peak values and change in their locations. The effect is more significant for smaller z_o/R_o. Again, the case of $z_o/R_o = 0.5$ shows a special interest because the effect of mismatch on the coupling efficiency is minimal in this case. Experimental data for the coupling efficiency was obtained, as shown in Fig. 7(b), using the measurement technique presented in Sec. 3. Spherical micromirrors with tangential and sagittal radii of curvatures of 200 and 100 μm, respectively, were used in this experiment. The height of the micromirrors is 150 μm, and their width is 400 μm. The micromirrors are aluminum metalized and have a reflectance of about 92%, which was used to extract their coupling efficiency with the aid of Eq. (19).

The coupling loss (in dB) versus the mismatch of the curvature $\Delta R/R$ is shown in Fig. 7(c) for different z_o/R. On one hand, the loss represented by dashed lines is obtained by dividing the

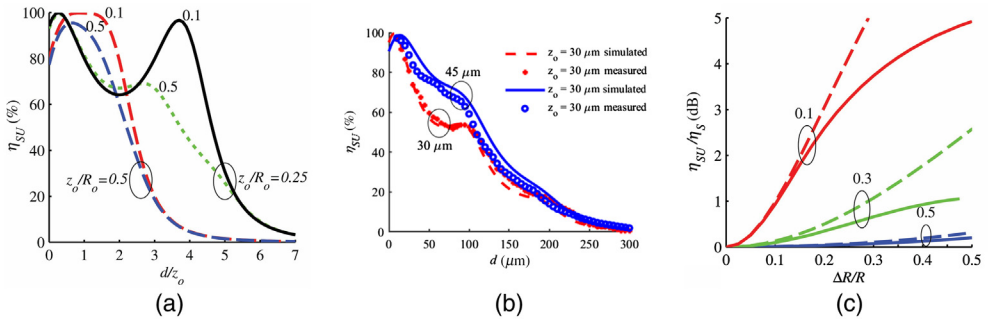

Fig. 7 Coupling efficiency of asymmetrical spherical micromirrors. (a) Theoretical data for different z_o/R ratios when $\Delta R/R = 0.1$ and 0.5. (b) Experimental data $R = 150$ μm and $\Delta R = 100$ μm when $z_o = 30$ and 45 μm. (c) Loss in coupling efficiency due to asymmetry in the micromirror curvature for different z_o/R ratios.

maximum value of the ideal coupling efficiency, which is unity, by the maximum value of reduced coupling efficiency due to mismatch. It is worth noting that the location of the maximum value can be different for the ideal and the reduced coupling efficiencies. On the other hand, the loss represented by solid lines is obtained by evaluating the reduced coupling efficiency at $d = 0.5R$ for the case of $z_o/R = 0.5$ and at $d = R$ for the other cases, regardless of the location of the peak. Despite of the fact that the maximum value of the coupling efficiency is reduced, an asymmetrical micromirror with mismatched radii of curvature provides a method to profile the coupling efficiency curve. For instance, consider the case of $z_o/R = 0.25$ in Fig. 7(a). The coupling efficiency curve for $\Delta R/R = 0.5$ has higher values in the range $d/z_o = 1$ to 3 than the symmetrical micromirror case.

In addition to asymmetry in the spherical micromirror surface, the micromachining and assembly of the micro-optical systems may result in misalignment between the incident beam axis and the optical axis of the micromirror. For the particular case of small misalignment with a spherical micromirror, Eq. (21) can be put in the form

$$\eta_{SM} = \eta_S \exp\left[-2\frac{\Delta_c^2}{w_o^2}\frac{1+(1-2d/R)^2+4(z_o/R)^2}{2+2(1-2d/R)^2+4(z_o/R)^2+(d/z_o)^2(1-d/R)^2}\right.$$
$$\left.-2\frac{\alpha_c^2}{\theta_o^2}\frac{(d/z_o)^2(1-d/R)^2+(1-2d/R)^2}{1+(d/z_o)^2(1-d/R)^2+(1-2d/R)^2}\right]. \tag{31}$$

The impact of lateral shift misalignment on the coupling efficiency was studied for $z_o/R_o = 0.5$ and 0.25; each with a shift $\Delta y/w_o = 0.1$, 0.3, and 0.5. The corresponding factors Δ_c/w_o and α_c/θ_o were deduced from the problem geometry to be $2(\Delta y/w_o)(d/R)$ and $2(\Delta y/w_o)(z_o/R)$, respectively. The corresponding coupling efficiency curves are shown in Fig. 8(a). Close to the micromirror surface; i.e., $d = 0$, the effect of misalignment is worse for $z_o/R_o = 0.5$. On the other hand, the effect is less pronounced around the peak value of the coupling efficiency. In addition, the misalignment causes a small shift in the peak location to be closer to the micromirror surface. This is referred to as the decaying behavior of the misaligned coupling efficiency with distance. Ignoring this small shift and focusing on the loss factor given by the exponential term in Eq. (31), the coupling loss (in dB) is shown in Fig. 8(b) versus the relative shift misalignment. The loss for $z_o/R_o = 0.5$, which is evaluated at $d = 0.5R$, has the advantage of being less affected by lateral misalignment and tolerates almost double the misalignment of other cases, which are evaluated at $d = R$. Apart from this case when $z_o/R_o < 0.5$, the loss is more pronounced for larger z_o/R_o, and the dependence on z_o/R_o is weak as long as the misalignment is not relatively large.

The impact of tilt misalignment on the coupling efficiency was studied for $z_o/R_o = 0.5$ and 0.25; each with a relative tilt $\Delta\theta/\theta_o = 0.1$, 0.3, and 0.5. Δ_c/w_o and α_c/θ_o were deduced from the problem geometry to be $2(\Delta\theta/\theta_o)(d/z_o)(1-d/R)$ and $2(\Delta\theta/\theta_o)(1-d/R)$, respectively. The corresponding coupling efficiency curves are shown in Fig. 8(c). Tilt misalignment hardly affects the case of $z_o/R_o = 0.25$ (or smaller) around $d = R$. Indeed, the tilt misalignment factors are null at $d = R$ because of the fact that a ray passing through the spherical micromirror center

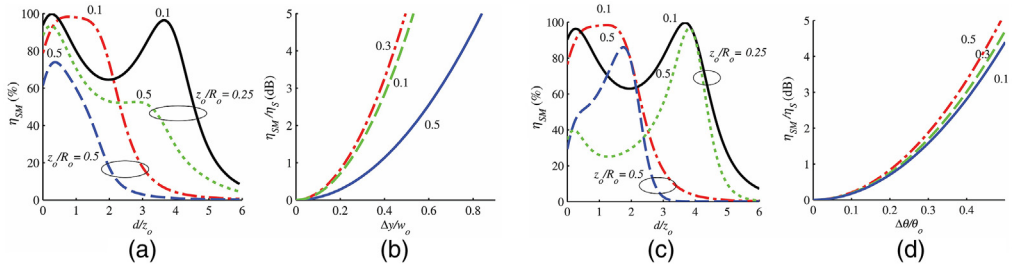

Fig. 8 Theoretical coupling efficiency of spherical micromirrors in the presence of misalignment. (a) Effect of shift for different z_o/R ratios when $\Delta y/w_o = 0.1$ and 0.5. (b) Loss in coupling efficiency due to shift misalignment for different z_o/R ratios. (c) Effect of tilt for different z_o/R ratios when $\Delta\theta/\theta_o = 0.1$ and 0.5. (d) Loss in coupling efficiency due to tilt misalignment for different z_o/R ratios.

of curvature will reflect back on itself whatever its tilt angle with respect to another reference axis passing through the center. It is also noteworthy that the original power coupling coefficient itself in Eq. (20) has a peak value that is slightly less than unity around $d = R$ and becomes closer to unity for smaller z_o/R_o. In contrast to the shift misalignment, tilt causes a small shift in coupling peaks toward larger d locations; i.e., away from the micromirror surface. The misalignment has its maximum impairment occurring close to $d = 0$ and is larger for larger z_o/R_o as shown in Fig. 8(d). From the results depicted in Figs. 8(a) and 8(c), one can conclude that, during the process of microassembly and alignment, each source of misalignment can be minimized in the zone where its effect is dominant. The tilt angle should be adjusted when the coupling distance is short enough, whereas the shift misalignment should be adjusted when the coupling distance is moderate, preferably at the location where the coupling efficiency is maximized.

5 Conclusion

Free-space coupling of Gaussian beams using silicon-etched micromirrors was analyzed thoroughly in this paper. A transfer matrix-based field and power coupling coefficients were derived for general micro-optical systems accounting for different matrix parameters in the tangential and sagittal planes of the microsystem. The derived expressions account for possible optical beam truncation due to the limited size of the micromirrors, rotational asymmetry in the curvature of the micromirrors and misalignments between the incident beam optical axis and the micromirror axis. The derived formulas were used to study the specific cases of flat (1D), cylindrical (2D), and spherical (3D) micromirrors. A measurement method based on using cleaved non-coated SM optical fibers was developed and applied to verify the theoretical analysis. Gaussian beams with $z_o = 30$ and 45 μm were used in the experiments. For micromirrors heights of w_o, $2w_o$, and $4w_o$, the truncation loss is significant for the first two cases, whereas its effect can be neglected for the third case, unless $d > 1.5z_o$. The non-monotonic coupling efficiency curve for cylindrical micromirrors is encountered when $R > 4z_o$, where R is the radius of curvature of the micromirror. Significant retrograding is, however, not possible, leading to poor coupling away from the micromirror surface. Spherical micromirrors were found to be efficient in Gaussian beam coupling when the $R > 2z_o$, such that 100% coupling efficiency is obtainable. The widest coupling efficiency response is obtained when $z_o/R = 0.5$. Asymmetry in the curvature of the spherical micromirrors in two orthogonal planes causes deterioration in the coupling efficiency, which is strongly dependent on the z_o/R ratio, similar to misalignment. But in some particular situations, asymmetry may improve the coupling efficiency. The effect of tilt misalignment is significant when the incident beam waist is in the vicinity of the spherical micromirror surface, whereas for shift misalignment it is significant for relatively large separation distance.

Acknowledgments

The authors declare no conflicts of interest.

References

1. S. S. Lee, L. Y. Lin, and M. C. Wu, "Surface-micromachined free-space micro-optical systems containing three-dimensional micrograting," *Appl. Phys. Lett.* **67**, 2135 (1995).
2. L. Y. Lin et al., "Surface-micromachined micro-xyz stages for free-space micro-optical bench," *IEEE Photonics Technol. Lett.* **9**, 345 (1997).
3. J. M. Bustillo, R. T. Howe, and R. S. Muller, "Surface micromachining for microelectromechanical systems," *Proc. IEEE* **86**, 1552 (1998).
4. M. Malak et al., "Micromachined Fabry–Perot resonator combining submillimeter cavity length and high quality factor," *Appl. Phys. Lett.* **98**, 211113 (2011).
5. M. Malak et al., "All-silicon Michelson instrument on chip: distance and surface profile measurement and prospects for visible light spectrometry," *Appl. Phys. Lett.* **102**, 141102 (2013).

6. C. Zener, "Internal friction in solids. Pt. II: General theory of thermoelastic internal friction," *Phys. Rev.* **53**, 90 (1938).
7. O. Arcizet et al., "Radiation-pressure cooling and optomechanical instability of a micromirror," *Nature (London)* **444**, 71 (2006).
8. F. Marty et al., "Advanced etching of silicon based on deep reactive ion etching for silicon high aspect ratio microstructures and three-dimensional micro-and nanostructures," *Microelectr. J.* **36**, 673 (2005).
9. Y. M. Sabry, D. Khalil, and T. Bourouina, "Monolithic silicon-micromachined free-space optical interferometers on chip," *Laser Photonics Rev.* **9**, 1 (2015).
10. C. Marxer et al., "Vertical mirrors fabricated by deep reactive ion etching for fiber-optic switching applications," *J. Microelectromech. Syst.* **6**, 277 (1997).
11. C. Marxer and N. F. de Rooij, "Micro-opto-mechanical 2×2 switch for single-mode fibers based on plasma-etched silicon mirror and electrostatic actuation," *J. Lightwave Technol.* **17**, 2 (1999).
12. B. Saadany et al., "A MEMS tunable optical filter based on vertical DBR architecture," in *Symp. Design, Test, Integr. and Packaging of MWMS/MOEMS*, p. 317 (2004).
13. B. Saadany et al., "Free-space tunable and drop optical filters using vertical Bragg mirrors on silicon," *IEEE J. Sel. Top. Quantum Electron.* **12**, 1480 (2006).
14. J. Masson et al., "Tunable fiber laser using a MEMS-based in plane Fabry–Pérot filter," *IEEE J. Quantum Electron.* **46**, 1313 (2010).
15. O. Manzardo et al., "Miniature lamellar grating interferometer based on silicon technology," *Opt. Lett.* **29**, 1437 (2004).
16. D. Khalil et al., "Miniaturized tunable integrated Mach–Zehnder MEMS interferometer for spectrometer applications," *Proc. SPIE* **7594**, 75940T (2010).
17. H. Omran et al., "Fully integrated Mach–Zhender MEMS interferometer with two complementary outputs," *IEEE J. Quantum Electron.* **48**, 244 (2012).
18. B. Saadany et al., "MEMS tunable Michelson interferometer with robust beam splitting architecture," in *IEEE/LEOS Int. Conf. Opt. MEMS and Nanophotonics*, p. 49 (2009).
19. Y. Sabry et al., "Optical characterization technique for MEMS comb-drive resonators," in *IEEE/LEOS Int. Conf. Opt. MEMS and Nanophotonics*, p. 127 (2009).
20. R. R. Syms and A. Lohmann, "MOEMS tuning element for a Littrow external cavity laser," *J. Microelectromech. Syst.* **12**, 921 (2003).
21. A. Q. Liu and X. M. Zhang, "A review of MEMS external-cavity tunable lasers," *J. Micromech. Microeng.* **17**, R1 (2007).
22. O. Manzardo et al., "Miniaturized time-scanning Fourier transform spectrometer based on silicon technology," *Opt. Lett.* **24**, 1705 (1999).
23. K. Yu et al., "Micromachined Fourier transform spectrometer on silicon optical bench platform," *Sens. Actuators A-Phys.* **130**, 523 (2006).
24. D. Khalil et al., "Characterization of MEMS FTIR spectrometer," *Proc. SPIE* **7930**, 79300J (2001).
25. Y. M. Sabry et al., "Integrated wide-angle scanner based on translating a curved mirror of acylindrical shape," *Opt. Express* **21**, 13906 (2013).
26. H. V. Jansen et al., "Black silicon method X: a review on high speed and selective plasma etching of silicon with profile control: an in-depth comparison between Bosch and cryostat DRIE processes as a roadmap to next generation equipment," *J. Micromech. Microeng.* **19**, 033001 (2009).
27. X. M. Zhang et al., "Discrete wavelength tunable laser using microelectromechanical systems technology," *Appl. Phys. Lett.* **84**, 329 (2004).
28. Y. Uenishi, K. Honma, and S. Nagaoka, "Tunable laser diode using a nickel micromachined external mirror," *IEEE Electron. Lett.* **32**, 1207 (1996).
29. S. S. Yun, S. K. You, and J. H. Lee, "Fabrication of vertical optical plane using DRIE and KOH crystalline etching of (110) silicon wafer," *Sens. Actuators A-Phys.* **128**, 387 (2006).
30. R. Agarwal, S. Samson, and S. Bhansali, "Fabrication of vertical mirrors using plasma etch and KOH: IPA polishing," *J. Micromech. Microeng.* **17**, 26 (2007).
31. D. Lee et al., "Vertical mirror fabrication combining KOH etch and DRIE of (110) silicon," *J. Microelectromech. Syst.* **18**, 217 (2009).

32. K. Khalil et al., "In-line optical MEMS phase modulator and application in ring laser frequency modulation," *IEEE J. Quantum Electron.* **52**, 5600108 (2016).
33. R. R. A. Syms and A. Lohmann, "MOEMS tuning element for a Littrow external cavity laser," *J. Microelectromech. Syst.* **12**, 921 (2003).
34. N. Gaber et al., "Optofluidic Fabry-Pérot micro-cavities comprising curved surfaces for homogeneous liquid refractometry—design, simulation, and experimental performance assessment," *Micromachines* **7**(4), 62 (2016).
35. E. Geerlings et al., "Widely tunable micro-mechanical external-cavity diode laser emitting around 2.1 μm," *IEEE J. Quantum Electron.* **44**, 1071 (2008).
36. D. C. Flanders et al., "Mounting and alignment structures for optical components," US patent 6,625,372 (2003).
37. K. Do et al., "Micro optical bench for mounting precision aligned optics, optical assembly and method of mounting optics," US patent 6,775,076 (2005).
38. Y. M. Sabry et al., "Silicon micromirrors with three-dimensional curvature enabling lens-less efficient coupling of free-space light," *Light Sci. Appl.* **2**, e94 (2013).
39. Y. Sabry et al., "In-plane diffraction loss free optical cavity using coated optical fiber and silicon micromachined spherical mirror," *Proc. SPIE* **8616**, 86160P (2013).
40. K. S. Chen et al., "Effect of process parameters on the surface morphology and mechanical performance of silicon structures after deep reactive ion etching (DRIE)," *J. Microelectromech. Syst.* **11**, 264 (2002).
41. H. C. Liu, Y. H. Lin, and W. Hsu, "Sidewall roughness control in advanced silicon etch process," *Microsyst. Technol.* **10**, 29 (2003).
42. W. H. Juan and S. W. Panga, "Controlling sidewall smoothness for micromachined Si mirrors and lenses," *J. Vac. Sci. Technol. B* **14**, 4080 (1996).
43. M.M. Lee and M. Wu, "Thermal annealing in hydrogen for 3D profile transformation on silicon on insulator and sidewall roughness reduction," *J. Microelectromech. Syst.* **15**, 338 (2006).
44. A. A. Avon, R. L. Bayt, and K. S. Breuer, "Deep reactive ion etching: a promissing technology for micro and nanosatellites," *Smart Mater. Struct.* **10**, 1135 (2001).
45. I. H. Song, Y. A. Peter, and M. Meunier, "Smoothing dry-etched microstructure sidewalls using focused ion beam milling for optical applications," *J. Micromech. Microeng.* **17**, 1593 (2007).
46. A. Lipson and E. M. Yeatman, "A 1-D photonic band gap tunable optical filter in (110) silicon," *J. Microelectromech. Syst.* **16**, 521 (2007).
47. J. Stone and D. Marcuse, "Ultrahigh finesse fiber Fabry–Perot interferometers," *J. Lightwave Technol.* **4**, 382 (1986).
48. D. Hunger et al., "A fiber Fabry–Perot cavity with high finesse," *New J. Phys.* **12**, 065038 (2010).
49. S. S. Lee et al., "Free-space fiber-optic switches based on MEMS vertical torsion mirrors," *J. Lightwave Technol.* **17**, 7 (1999).
50. J. Holm et al., "Through-etched silicon carriers for passive alignment of optical fibers to surface-active optoelectronic components," *Sens. Actuators A-Phys.* **82**, 245 (2000).
51. K. Ishikawa et al., "An integrated micro-optical system for VCSEL-to-fiber active alignment," *Sens. Actuators A-Phys.* **103**, 109 (2003).
52. Q. X. Zhang et al., "A silicon platform with MEMS active alignment function and its potential application in Si-photonics packaging," *IEEE J. Sel. Top. Quantum Electron.* **16**, 267 (2010).
53. D. Marcuse, "Loss analysis of single-mode fiber splices," *Bell Syst. Tech. J.* **56**, 703 (1977).
54. W. B. Joyce and B. C. DeLoach, "Alignment of Gaussian beams," *Appl. Opt.* **23**, 4187 (1984).
55. S. Sarkar, K. Thyagarajan, and A. Kumar, "Gaussian approximation of the fundamental mode in single mode elliptic core fibers," *Opt. Commun.* **49**, 178 (1984).
56. B. Hillerich, "Shape analysis and coupling loss of microlenses on single-mode fiber tips," *Appl. Opt.* **27**, 3102 (1988).
57. S. Gangopadhyay and S. Sarkar, "ABCD matrix for reflection and refraction of Gaussian light beams at surfaces of hyperboloid of revolution and efficiency computation for laser

diode to single-mode fiber coupling by way of a hyperbolic lens on the fiber tip," *Appl. Opt.* **36**, 8582 (1997).
58. S. Yuan and N. A. Riza, "General formula for coupling-loss characterization of single-mode fiber collimators by use of gradient-index rod lenses," *Appl. Opt.* **38**, 3214 (1999).
59. R. R. A. Syms. "Principles of free-space optical microelectromechanical systems," *Proc. Inst. Mech. Eng., Part C: J. Mech. Eng. Sci.* **222**, 1 (2008).
60. Y. M. Sabry et al., "In-plane optical beam collimation using a three-dimensional curved MEMS mirror," *Micromachines* **8**, 134 (2017).
61. L. Jing and A-Q. Liu. "Design of MEMS optical switches," in *Photonic MEMS Devices: Design, Fabrication and Control*, p. 27 (2018).
62. M. A. Basha, A. Rohani, and S. Safavi-Naeini. "A fast method for analysis and modeling of optical MEMS switches," in *Microelectromech. Syst. Conf. (Cat. No. 01EX521)*, IEEE, p. 54 (2001).
63. J. Li, Q. X. Zhang, and A. Q. Liu, "Advanced fiber optical switches using deep RIE (DRIE) fabrication," *Sens. Actuators A-Phys.* **102**, 286 (2003).
64. T. S. Lim et al., "Electrostatic MEMS variable optical attenuator with rotating folded micro-mirror," *IEEE J. Sel. Top. Quant. Electron* **10**, 558 (2004).
65. B. Saadany et al., "A miniature Michelson interferometer using vertical Bragg mirrors on SOI," in *IEEE/LEOS Int. Conf. Opt. MEMS and Their Appl. Conf.*, p. 50 (2006).
66. Y. M. Sabry et al., "In-plane deeply-etched optical MEMS notch filter with high-speed tenability," *J. Opt.* **17**, 125703 (2015).
67. M. Erfan et al., "On-chip micro–electro–mechanical system Fourier transform infrared (MEMS FT-IR) spectrometer-based gas sensing," *Appl. Spectrosc.* **70**, 897–904 (2016).
68. A. Fathy et al., "Silicon multi-pass gas cell for chip-scale gas analysis by absorption spectroscopy," *Micromachines* **11**, 463 (2020).
69. H. Omran et al., "Visible laser on silicon optofluidic microcavity," *Adv. Mater. Technol.* **5**, 1901132 (2020).
70. M. A. Othman et al., "Modal analysis of TE and TM excitations in a metallic slotted micro-mirror," *J. Opt. Soc. Am. B* **36**, 610 (2019).
71. Z. Moktadir et al., "Etching techniques for realizing optical micro-cavity atom traps on silicon," *J. Micromech. Microeng.* **14**, S82 (2004).
72. N. Kanbara, S. I. Tezuka, and T. Watanabe, "MEMS tunable VCSEL with concave mirror using the selective polishing method," in *Proc. IEEE Opt. MEMS*, p. 9 (2006).
73. Y. Ow, M. B. H. Breese, and S. Azimi, "Fabrication of concave silicon micro-mirrors," *Opt. Express* **18**(14), 14511 (2010).
74. X. Wang et al., "Spherical concave micro-mirror fabricated using gray-tone optical lithography for vertical coupling," *Opt. Express* **29**(9), 13288–13301 (2021).
75. P. Goldsmith, *Quasioptical Systems: Gaussian Beam Quasi-Optical Propagation and Applications*, Wiley-IEEE Press, New York (1997).
76. N. Hodgson and H. Weber, *Laser Resonators and Beam Propagation: Fundamentals, Advanced Concepts and Applications*, Springer-Verlag New York, LLC (2005).
77. O. Solgaard, *Photonic Microsystems: Micro and Nanotechnology Applied to Optical Devices and Systems*, Springer (2008).
78. H. T. Yura and T. S. Rose, "Gaussian beam transfer through hard-aperture optics," *Appl. Opt.* **34**, 6826 (1995).
79. S. O. Rice, "Reflection of electromagnetic waves from slightly rough surfaces," *Commun. Pure Appl. Math.* **4**, 351 (1951).
80. H. Davies, "The reflection of electromagnetic waves from a rough surface," in *Proc. IEE-Part IV: Inst. Monogr.*, Vol. 101, p. 209 (1954).
81. P. Beckmann and A. Spizzichino, *The Scattering of Electromagnetic Waves from Rough Surfaces*, Pergamon Press (1963).
82. J. E. Harvey, "Light-scattering characteristics of optical surfaces," PhD thesis, University of Arizona (1976).
83. J. E. Harvey, N. Choi, and A. Krywonos, "Scattering from moderately rough interfaces between two arbitrary media," *Proc. SPIE* **7794**, 77940V (2010).

84. T. V. Vorburger, E. Marx, and T. R. Lettieri, "Regimes of surface roughness measurable with light scattering," *Appl. Opt.* **32**, 3401 (1993).
85. C. K. Carniglia and D. G. Jensen, "Single-layer model for surface roughness," *Appl. Opt.* **41**, 3167 (2002).
86. R. St-Gelais, A. Poulin, and Y. A. Peter, "Advances in modeling, design, and fabrication of deep-etched multilayer resonators," *J. Lightwave Technol.* **30**, 1900 (2012).
87. A. W. Snyder and J. D. Love, *Optical Waveguide Theory*, Chapman and Hall, London (1983).

Yasser M. Sabry received his BSc and MSc degrees (with honors) in electrical engineering from Ain Shams University, Cairo, Egypt, in 2005 and 2009, respectively. He obtained his PhD from the Université Paris-Est (currently Gustave Eiffel), ESIEE Paris, France, in 2013. He received the TWAS-ARO Young Arab Scientist prize and Egypt State Encouragement Award in Engineering Science. He is currently an associate professor at Ain Shams University, Egypt, and the head of Optical and Microsystems Technologies Group in Si-Ware Inc. He is the principal inventor of the Neospectra Micro optical solution. His current research interests include spectral sensors and solutions, microphotonics, biophotonics, and artificial intelligence.

Mazen Erfan received his BSc (with honors) and MSc degrees in electrical engineering from Ain Shams University, Cairo, Egypt, in 2012 and 2016, respectively. He obtained his PhD from the Université Paris-Est (currently Gustave Eiffel), ESIEE Paris, France, in 2019 and was the winner of the Best PhD Business Thesis Prize 2020 among the university awarded by Descartes Développement & Innovation (DD&I). He is currently an assistant professor at Ain Shams University, Egypt. His research interests include microsystems, micro-photonics, optofluidics, optical MEMS, and nanomaterials.

Diaa Khalil has over 35 years of experience in micro photonics systems. He obtained his PhD from INPG France in 1993. He is a professor of photonics in ASU since 2004. He also served as acting dean and vice dean of PG and research in the School of Engineering, ASU. From 2007 to 2020, he was the CTO of the Optical MEMS Division in Si-Ware Systems, leading a group developing an innovative MEMS spectrometer that gained the Prism award in the Photonics West conference 2014 in SF USA. He received the Egyptian state incentive prize in engineering sciences in 1998. He is inventor of about 25 patents and patent applications and the author and co-author of more than 370 publications, 3 book chapters, and 1 ebook. He is a member of the editorial board of the *Light: Science and Applications* journal, produced by the Nature PG.

Tarik Bourouina obtained his PhD in 1991 and his Habilitation (HDR) in 2000 from the Université Paris-Saclay. He has been professor of physics at ESIEE Paris, Université Gustave Eiffel since 2002. Currently, he is dean for Research of ESIEE Paris. He is affiliated with the French National Center for Scientific Research (CNRS) within the ESYCOM laboratory UMR9007. He was previously senior research fellow at the University of Tokyo, Japan, and associate professor at the Université Paris-Saclay, France. Since 2007, he has been the advisory CSO of the MEMS division at Si-ware Systems and is co-founder of Fluidion in 2012 and Izonics in 2021. In 2017, he was the recipient of the Chinese Academy of Sciences President's Fellowship.